JACS Au
AN OPEN ACCESS JOURNAL OF THE AMERICAN CHEMICAL SOCIETY

pubs.acs.org/jacsau

Article

Insights into the Interaction between Immobilized Biocatalysts and Metal−Organic Frameworks: A Case Study of PCN-333

Wenjie Yang, Weibin Liang,* Luke A. O'Dell, Hamish D. Toop, Natasha Maddigan, Xingmo Zhang, Alena Kochubei, Christian J. Doonan, Yijiao Jiang, and Jun Huang*

Cite This: *JACS Au* 2021, 1, 2172−2181

Read Online

ACCESS | Metrics & More | Article Recommendations | Supporting Information

ABSTRACT: The immobilization of enzymes in metal−organic frameworks (MOFs) with preserved biofunctionality paves a promising way to solve problems regarding the stability and reusability of enzymes. However, the rational design of MOF-based biocomposites remains a considerable challenge as very little is known about the state of the enzyme, the MOF support, and their host−guest interactions upon immobilization. In this study, we elucidate the detailed host−guest interaction for MOF immobilized enzymes in the biointerface. Two enzymes with different sizes, lipase and insulin, have been immobilized in a mesoporous PCN-333(Al) MOF. The dynamic changes of local structures of the MOF host and enzyme guests have been experimentally revealed for the existence of the confinement effect to enzymes and van der Waals interaction in the biointerface between the aluminum oxo-cluster of the PCN-333 and the -NH_2 species of enzymes. This kind of host−guest interaction renders the immobilization of enzymes in PCN-333 with high affinity and highly preserved enzymatic bioactivity.

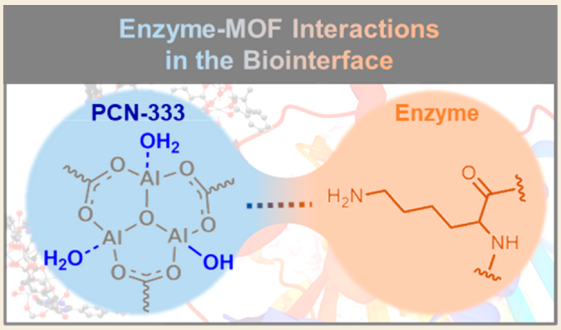

KEYWORDS: *metal−organic frameworks, enzyme immobilization, solid-state NMR, biointerface interaction, biocatalysis*

INTRODUCTION

Metal−organic frameworks (MOFs) are a class of extended network materials constructed from a bottom-up building block approach by connecting metal-based clusters and organic ligands.[1−3] MOFs are well-known for their high degree of crystallinity, remarkable surface areas and pore volumes, and structural tunability.[4,5] These design features have motivated researchers from a broad range of scientific and engineering disciplines to explore the fundamental and applied aspects of MOF materials.[6] Recently, the area of enzyme/MOF biocomposites has experienced considerable growth due to their potential applications in biotechnology.[7,8] Biomolecules can interact with MOFs via a wide variety of interactions including covalent attachment, coordination bonds, hydrogen bonding, $\pi-\pi$ and hydrophobic interactions, and electrostatic attraction.[9] The most widely employed strategy to synthesize enzyme/MOF biocomposites is to infiltrate the biomacromolecule within the MOF pore network.[10] Due to their modular construction and chemical mutability,[11] MOFs allow for their pore environment to be optimized to house specific proteins to a level of precision that is not attainable for other porous materials,[12,13] such as silica matrixes,[14] organic polymers,[15] and DNA-based compartments.[16] To date, these MOF-based biocomposites have been explored for applications in biocatalysis,[7] biomedicine,[17] controlled release and drug delivery,[18] biopreservation,[19] and cell and virus manipulation.[8]

However, the majority of studies, nowadays, have focused on the synthesis and performance characteristics of enzyme/MOF biocomposites;[20,21] little is known about the fundamental molecular interactions between the MOF and enzyme that govern the immobilization process. When an enzyme molecule is in contact with a MOF support, its structure, orientation, and conformational mobility can be modified, and this typically leads to a change in its native functionality such as a significant loss of catalytic activity.[22] Thus, to maintain the activity of enzymes immobilized within MOF pores a detailed understanding of the host−guest interactions is necessary. A number of characterization techniques have been employed to examine how MOF pore environment influences the structure of an enzyme,[23] including, circular dichroism (CD),[24] electron paramagnetic resonance (EPR),[25,26] diffuse reflectance infrared Fourier transform spectroscopy (DRIFTS),[21] and Raman spectroscopy.[27] In recent years, methodological developments have led solid-state nuclear magnetic resonance (ssNMR) to be one of the most powerful tools for determining the local structure and dynamics of various materials, including proteins,

Received: May 21, 2021
Published: November 15, 2021

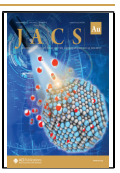

https://doi.org/10.1021/jacsau.1c00226
JACS Au 2021, 1, 2172−2181

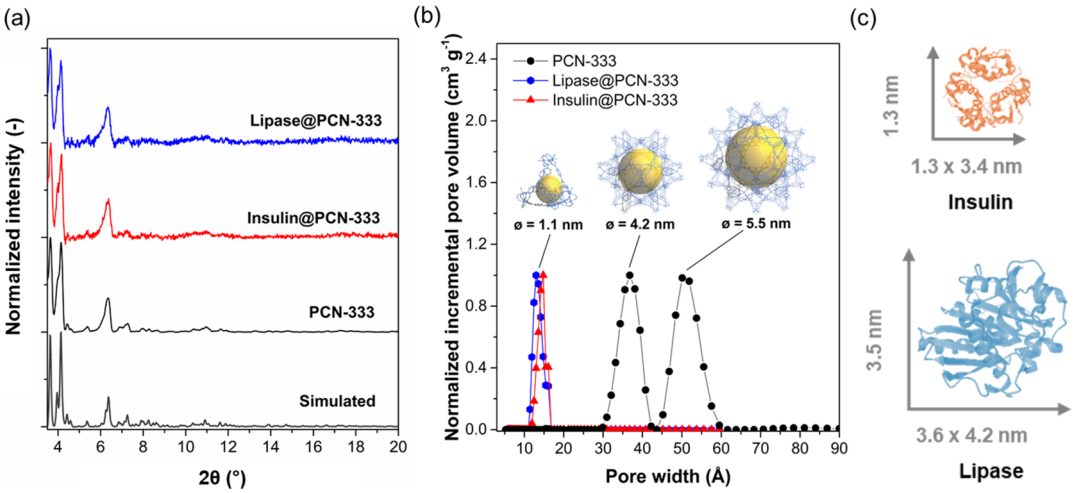

Figure 1. (a) Simulated (gray) and experimental PXRD patterns of PCN-333 (black), lipase@PCN-333 (blue), and insulin@PCN-333 (red). (b) Pore size distributions of PCN-333 (black), lipase@PCN-333 (blue), and insulin@PCN-333 (red). Pore size distributions were calculated using NLDFT model based on the N_2 adsorption isotherms measured at 77 K (Figure S1). The salient pore features of PCN-333 are shown as insets. (c) Molecular structure of insulin (PDB 2A3G, insulin from bovine pancreas) and lipase (PDB 1OIL, lipase from *Pseudomonas cepacia*).

catalysts, biomaterials, pharmaceuticals, metal−organic materials, and so on.[28−30] For example, Fragai et al.[31] showed that the three-dimensional structures of the enzymes were retained after immobilization in a peptide-templated silica gel. Indeed, ssNMR spectroscopy has been applied as a general approach to study MOFs and their interactions with small guest species[32] (e.g., H_2,[33] xenon,[34] CO,[35] CO_2,[36,37] nitric oxide,[38] H_2O,[39] hydrocarbon,[40] aromatics,[41,42] etc.), providing complementary information for host−guest interaction.[43] For example, with the help of ssNMR, the coordination of methanol to the open metal sites in $[Cu_{3-x}Zn_x(btc)_2]_n$ (btc = 1,3,5-benzenetricarboxylate) has been proven and unveiled in detail at an atomic level.[44] In another study, the interactions between the Cr of the host MOF (Cr-MIL-101) and guest molecules (e.g., water, 2-aminopyridine, 3-aminopyridine, and diethylamine) have been revealed by a combination of density functional theory (DFT) calculations and $^{13}C-^{1}H$ rotational-echo double-resonance (REDOR) NMR.[45] In addition, ssNMR is advantageous to probe the host−guest interaction in other porous materials such as zeolites,[46,47] amorphous silica−alumina,[48] and mesoporous organic materials.[49,50] However, ssNMR has not yet been employed to examine the atomic-level host−guest interactions in MOF-based biocatalysts.

In this work, we envision that comprehensive microscopy, ssNMR, and reaction study can provide data that will advance our fundamental understanding of the host−guest interactions in the enzyme−MOF biointerface allowing for these systems to be optimized for enhanced enzyme preservation and protection. Lipase and insulin were loaded in a mesoporous MOF, PCN-333(Al), to afford lipase@PCN-333 and insulin@PCN-333 biocatalysts. The routine characterizations (X-ray diffraction (XRD) and 77 K N_2 gas adsorption analysis) combined with scanning electron microscopy (SEM), confocal laser scanning microscopy (CLSM), and enzymatic tests have confirmed the successful immobilization of the targeted biocatalyst (lipase and insulin) in PCN-333. Furthermore, multinuclei 1D and 2D ssNMR and their multiple-quantum, double-resonance, and relaxation ssNMR measurements were employed to elucidate the local chemical environment and host−guest interactions between immobilized enzymes and the framework, PCN-333. The reaction results showed that the discovered host−guest interaction is able to confine the lipase inside PCN-333 while preserving its enzymatic bioactivity after immobilization.

RESULTS AND DISCUSSION

PCN-333 has been reported to exhibit high porosity and exceptional chemical stability. These physical characteristics endow PCN-333 as an excellent platform for biomolecule immobilization. PCN-333 has been synthesized using a variety of metal precursors to realize metal nodes based on aluminum (Al), iron (Fe), and scandium (Sc).[51] In this work, the Al version of PCN-333, PCN-333(Al), was selected for enzyme immobilization to facilitate the application of ssNMR techniques. The PCN-333 framework consists of $[Al_3(\mu_3\text{-}O)(OH)(H_2O)_2]^{6-}$ clusters (Al-oxo clusters) linked by tridentate TATB (4,4′,4″-*s*-triazine-2,4,6-triyl-tribenzoate) ligands, which form supertetrahedra (ST). These ST are connected via vertices to form a three-dimensional mtn network. This network topology affords two types of mesopores: a dodecahedral cage measuring 42 Å and a hexacaidecahedral cage measuring 55 Å (Figure 1b). PCN-333 was prepared and activated according to the literature procedure reported by Zhou et al.[51] The permanent porosity of PCN-333 was assessed by performing 77 K N_2 gas adsorption isotherms. Application of the Brunauer−Emmett−Teller (BET) equation to the isotherm data afforded a surface area of 4198 $m^2\ g^{-1}$ (Figure S1), which is consistent with the reported values.[51] Recent publications have reported the successful immobilization of different enzymes within the pore network of PCN-333, including horseradish peroxidase (HRP),[51] cytochrome c (Cyt c),[51] microperoxidase-11 (MP-11),[51] catalase (CAT),[52] superoxide dismutase (SOD),[52] and alcohol dehydrogenase (ADH).[53] In this study, we have selected two commercially available enzymes of different sizes for the immobilization experiments: lipase ($3.0 \times 4.0 \times 5.0\ nm^3$)[54] and insulin ($1.3 \times 1.3 \times 3.4\ nm^3$)[55] (Figure 1c). Lipase is a commercially important enzyme that catalyzes hydrolysis reactions,[56] and insulin is an important medical hormone responsible for regulating the concentration of glucose in blood plasma.[57] We note that both biomolecules, in their active conformation (in crystallographic dimensions), are

https://doi.org/10.1021/jacsau.1c00226
JACS Au 2021, 1, 2172−2181

smaller than that of the largest mesopore (ø = 5.5 nm) in PCN-333 (Figure 1b) and, thus, in principle, can infiltrate the MOF pores.

To immobilize the selected enzymes, PCN-333 crystals were soaked in an aqueous solution of lipase or insulin for 1 h at 4 °C (see Experimental Section for details). Control experiments confirmed the integrity of PCN-333 under these immobilization conditions (Figure S5). The resulting MOF-based biocatalysts were washed with water three times to remove the excess or loosely absorbed enzyme species on the MOF surface, affording biocatalysts denoted as lipase@PCN-333 and insulin@PCN-333. The loadings of lipase and insulin in lipase@PCN-333 and insulin@PCN-333 ($P_{loading}$[10]) were calculated to be 26.9 and 50.0 mg g^{-1}, respectively (Bradford assay,[58] Figure S2). The values of loading efficiency (Y_P[10]) were then determined to be 53.8% and 100% for lipase and insulin, respectively. To determine if PCN-333 retained bulk crystallinity subsequent to the infiltration process, we performed powder X-ray diffraction (PXRD) measurements. Figure 1a shows that the PXRD patterns of both the lipase and insulin biocomposites are essentially identical to pristine PCN-333. The porosity of the biocomposites was examined by carrying out N_2 77 K gas adsorption isotherms. As anticipated, the total N_2 uptakes for lipase@PCN-333 and insulin@PCN-333 decrease significantly as compared to that of PCN-333 (Figure S1). In addition, the normalized pore size distributions calculated via the nonlinear density function theory (NLDFT) show a disappearance of mesoporosity in lipase@PCN-333 and insulin@PCN-333 (Figure 1b). These results can be rationalized by the presence of large biomolecules (lipase or insulin) within the mesopores of PCN-333. Attempts to characterize structural features of the encapsulated biomolecules within the enzyme@PCN-333 samples using attenuated total reflection Fourier transform infrared spectroscopy (ATR-FTIR) were unsuccessful due to the interference of PCN-333 background peaks (Figure S3).

We then applied scanning electron microscopy (SEM) to ascertain the crystal size and morphology of PCN-333 and the enzyme@PCN-333 biocomposites. Close inspection of the micrographs shows that PCN-333, lipase@PCN-333, and insulin@PCN-333 samples were dispersed octahedral crystals (~300 nm in diameter, Figure S4). The morphological homogeneity and crystal size triggered us to visualize the spatial distribution of lipase within PCN-333 using confocal laser microscopy (CLSM). In order to visualize the lipase within the biocomposite crystals using CLSM, a fluorescent tag needs to be attached to the enzyme. Fluorescein-tagged lipase (FITC-lipase) was prepared and used to synthesize FITC-lipase@PCN-333. The synthesis and washing protocol for FITC-lipase@PCN-333 were analogous to those of lipase@PCN-333. CLSM images (Figure S6) show that the FITC-lipase molecules were present throughout FITC-lipase@PCN-333 crystals; however, due to the resolution of this technique, we are unable to differentiate between signal from surface-absorbed FITC-lipase and encapsulated FITC-lipase. Supplementary experiments with HRP@PCN-333 confirmed the successful infiltration/encapsulation of the biomolecules within the mesopores of PCN-333 (Figures S13–S17).

To assess the enzymatic performance of the biocomposite, we measured the catalytic hydrolysis of *p*-nitrophenyl butyrate (PNPB) using free FITC-lipase and FITC-lipase@PCN-333 biocatalyst (Figure 2a). A noteworthy result is that FITC-lipase@PCN-333 showed comparable activity to that of free

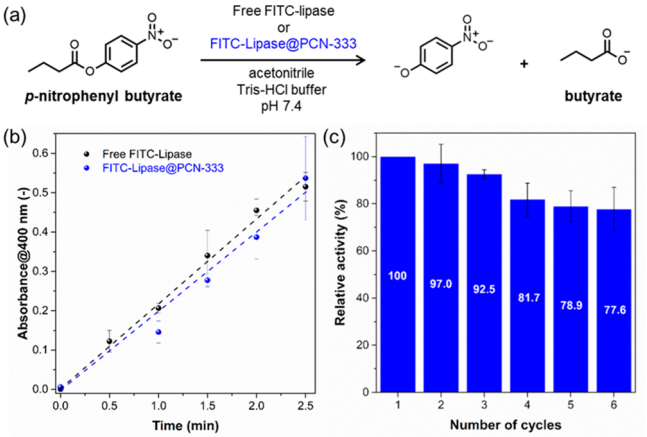

Figure 2. (a) Biocatalytic hydrolysis of *p*-nitrophenyl butyrate (PNPB). (b) Catalytic activity of FITC-lipase and FITC-lipase@PCN-333 biocomposite. The amount of FITC-lipase available was the same for each experiment (25 μg based on FITC-lipase). (c) Cycling runs for the hydrolysis of 4-nitrophenyl butyrate in the presence of FITC-lipase@PCN-333 after a reaction time of 2 min. Experiments were performed in triplicate with standard error bars shown for each run.

FITC-lipase (Figure 2b). Approximately 91.6% of the bioactivity (calculated based on the slope of the reaction kinetics) of FITC-lipase was retained upon immobilization in FITC-lipase@PCN-333.

Given that the catalytic activity of the immobilized lipase is preserved for FITC-lipase@PCN-333 (Figure 2b), we sought to examine recyclability, an important performance factor for practical applications. The relative bioactivity of FITC-lipase@PCN-333 biocomposites was calculated by comparing the relative activity with that of the first run. We successfully cycled FITC-lipase@PCN-333 six times with a 22.4% reduction in enzymatic activity in the sixth cycle (Figure 2c). This observed reduction is actually due to enzyme leaching from the FITC-lipase@PCN-333 samples during the washing procedure between cycles (Figure S7 and Table S1–S2). Interpreting these results, it is concluded that the lipase biomolecules retained their bioactivity and are confined in PCN-333 framework in relatively high affinity.

To elucidate the interactions between the enzyme and PCN-333, we studied PCN-333, lipase@PCN-333, and insulin@PCN-333 using ssNMR techniques. A unique characteristic of MOFs is that their structural flexibility enables their molecular architectures to exhibit local motions under external stimuli.[59,60] Upon pore-filling with large biomolecules, we anticipate a subtle difference in the local flexibility of the PCN-333 framework. Solid-state NMR has been proven to be a powerful tool to investigate the molecular dynamics in a variety of materials by applying relaxation or diffusion spectroscopy.[61−63] In this work, in order to understand the structural flexibility of the framework, the ^{1}H spin−lattice relaxation (^{1}H T_1) was measured by applying the inversion−recovery pulse sequence. For ^{1}H T_1 analysis, as the magnetization of ^{1}H nuclei can rapidly diffuse throughout the entire spin network of the solid, a relatively uniform T_1 value for all protons in the material is expected. In addition, due to the strong homonuclear dipolar−dipolar interactions and the high natural abundance of the ^{1}H nuclei, the ^{1}H T_1 value of the whole set of ^{1}H peaks can be utilized to represent the molecular dynamics of the entire network. Therefore, the peaks across the whole

https://doi.org/10.1021/jacsau.1c00226
JACS Au 2021, 1, 2172−2181

spectrum in the ^{1}H spectra obtained via the application of the inversion−recovery pulse sequence were selected to acquire the relaxation curves, and the ^{1}H T_1 values are obtained accordingly (Figure S8 and Table 1).

Table 1. Molecular Dynamics Measurements for PCN-333, Lipase@PCN-333, and Insulin@PCN-333 via ^{1}H and ^{27}Al Relaxation Spectroscopy

nuclei	materials	T_1 (ms)
^{1}H	PCN-333	936
	insulin@PCN-333	2323
	lipase@PCN-333	2342
^{27}Al	PCN-333	14.92
	insulin@PCN-333	11.23
	lipase@PCN-333	11.05

In general, increasing mobility in a solid will result in reduced ^{1}H spin−lattice relaxation times.[64] As shown in Table 1, after enzyme immobilization, lipase@PCN-333 and insulin@PCN-333 show a much longer spin−lattice relaxation time compared to PCN-333 (T_1 = 2.342, 2.323, and 0.936 s for insulin@PCN-333, lipase@PCN-333, and PCN-333, respectively, Table 1 and Figure S8a). These results indicate that the mobility of protons in lipase@PCN-333 and insulin@PCN-333 decreases as compared to those in PCN-333. Since these ^{1}H T_1 values reflect the flexibility of the entire network, a longer T_1 value indicates a reduction in local framework flexibility upon enzyme immobilization. This effect is expected and can be rationalized by the confinement of the large enzyme biomolecules in lipase@PCN-333 and insulin@PCN-333.[65] A similar phenomenon has been observed in the case of benzene loaded UiO-66(Zr), where a decrease in the internal dynamics of π-flips of the terephthalate ligands was observed.[41]

T_1 relaxation times of ^{27}Al were also measured with the purpose of comparing the local mobility of the Al sites in different PCN-333 samples. Interestingly, as shown in Table 1 and Figure S8b, after enzyme immobilization, a decrease in the ^{27}Al T_1 relaxation time is observed for both lipase@PCN-333 and insulin@PCN-333. The decrease, instead of increase, in the ^{27}Al T_1 relaxation times after enzyme immobilization clearly demonstrates that the local flexibility of Al centers in the PCN-333 framework has a different dynamic behavior compared with the entire framework (Table 1).[64] This observation points to the possible existence of interaction between the Al-oxo cluster and enzymes, which relax the existing coordination bonds of Al-oxo cluster in PCN-333 and contributed to a lower ^{27}Al T_1 value.

In order to further illustrate the structural change of PCN-333 after enzyme immobilization in detail and understand the nature of the host−guest interactions at the atomic scale, one-dimensional and two-dimensional ssNMR spectroscopies were conducted to investigate the local chemical structure of the PCN-333 biocomposites. The pristine PCN-333 (Figure 3) was first analyzed by ssNMR to establish a reference point. By application of ^{1}H and ^{13}C magic-angle spinning (MAS) NMR spectroscopy, all the proton and carbon species in PCN-333 (Figure 3) were successfully assigned. The broad ^{1}H signal at 7−9 ppm is partially attributed to the coordinated water on the trimeric Al-oxo cluster (Al···OH_2, denoted as H4 in Figure 3a), which shows a higher ppm value in comparison with that of the free H_2O ($\delta_{^{1}H}$ = ca. 5 ppm). This assignment is supported by recent ssNMR studies.[66,67] In one study of MIL-110, Haouas et al. reported a higher ^{1}H chemical shift value for the coordinated water ($\delta_{^{1}H}$ = 5.8 ppm) than that of the free water ($\delta_{^{1}H}$ = 4.4 ppm) in the framework.[66] In another case, the coordinated water (Al−H_2O) in mineral alunite signaled at a lower chemical field shift in the ^{1}H NMR spectrum ($\delta_{^{1}H} \approx$ 7.4 ppm) in comparison with the free H_2O (δ = 4.8 ppm).[67] In addition, these broad ^{1}H peaks ($\delta_{^{1}H}$ = 7−9 ppm) are associated with the aromatic C−H species (H1 and H2) of the TATB ligand (Figure 3a,b).[68] The ^{1}H signal at δ_{1H} = 2.4 ppm is assigned to the proton of the coordinated hydroxyl (H3, Figure 3a) species in the Al-oxo cluster ($Al_3(\mu_3\text{-}O)(OH)(H_2O)_2$).[69] A broad ^{1}H signal at around 5 ppm is assigned as the free H_2O molecule.[38,69] These assignments are consistent with an ssNMR study of MIL-100(Al).[69] However, no proton signal was identified in the region of ∼2 ppm for MIL-100(Al), as an extra-framework btc ligand instead of a hydroxyl group is present in MIL-100(Al) to balance the charge of the Al-oxo cluster. In another study, in the absence of extra-framework btc ligand in MIL-100(Al), hydroxyl protons (−OH) peaks appear at $\delta_{^{1}H}$ = 1.5 and 0.3 ppm.[38] Figure 3c (gray line) shows the ^{13}C CP MAS NMR spectra of the PCN-333 samples. The aromatic C2 and C5 of the TATB ligand can be observed at $\delta_{^{13}C}$ = 138 ppm, while C3 and C4 sit at $\delta_{^{13}C}$ = 129 ppm. Deconvolution of the broad peak at 170−174 ppm confirms the existence of the C1 ($\delta_{^{13}C}$ = 173 ppm) and C6 species ($\delta_{^{13}C}$ = 171 ppm) (Figure 3d and Table S3). Other small peaks originating from the

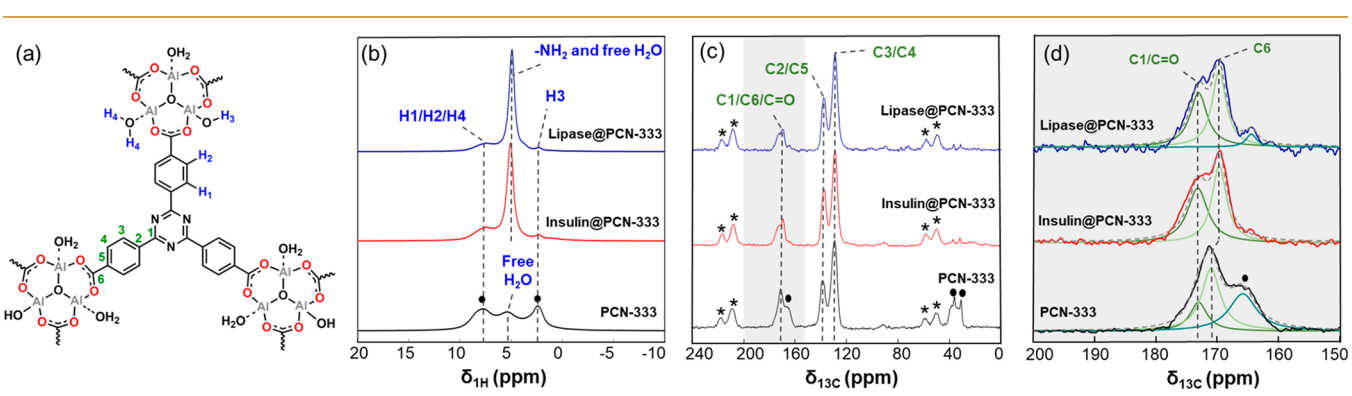

Figure 3. (a) Molecular representation of PCN-333(Al). (b) ^{1}H one-pulse MAS NMR spectra. (c) ^{13}C cross-polarization MAS NMR spectra of PCN-333 (black), lipase@PCN-333 (blue), and insulin@PCN-333 (red). Asterisks represent sidebands; filled circles indicate the residue solvent signals (DMF). (d) Deconvolution of ^{13}C peaks in the region of 150−200 ppm.

https://doi.org/10.1021/jacsau.1c00226
JACS Au 2021, 1, 2172−2181

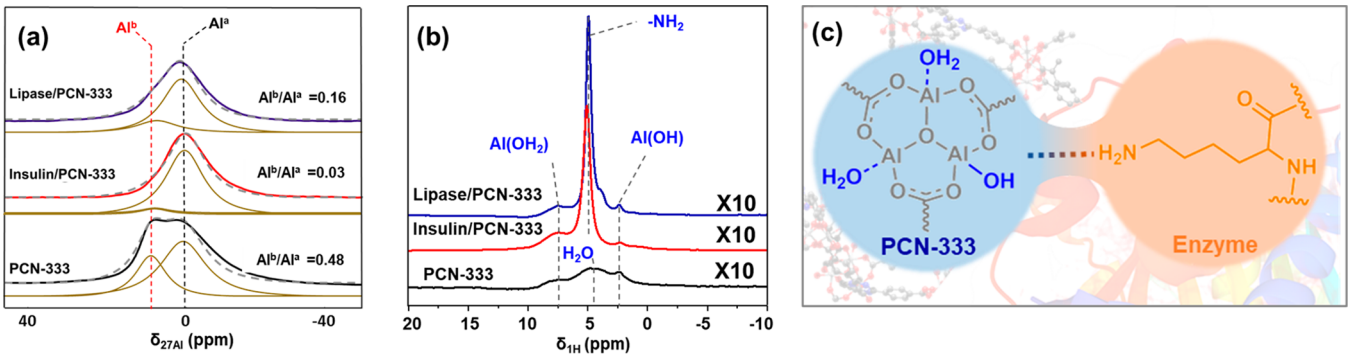

Figure 4. (a) Deconvolution of ^{27}Al MAS NMR spectra of PCN-333 samples. (b) ^{1}H/^{27}Al TRAPDOR difference spectra of PCN-333 samples (10 times amplified). (c) Schematic illustration of enzyme−PCN-333 interaction in the biointerface.

residue solvent were also observed (*N*,*N*′-dimethylformamide (DMF), Figure 3b,c).[70]

After enzyme immobilization, a drastic change in the ^{1}H spectra can be observed for enzyme@PCN-333 as compared to that of PCN-333 (Figure 3b). In lipase@PCN-333 and insulin@PCN-333, a sharp ^{1}H signal emerges at 5 ppm (Figure 3b). The sharp ^{1}H signal ($\delta_{^{1}H}$ = 5 ppm) can also be identified in ^{1}H MAS NMR spectra of free enzymes (Figure S9). Compared to the broad water proton signal in PCN-333 ($\delta_{^{1}H} \approx 5$ ppm, Figure 3b), the sharp ^{1}H peak centered at 5 ppm for lipase@PCN-333 and insulin@PCN-333 can be assigned to the -NH_2 species (Figure 3b) in enzyme biomolecules[69] and the free H_2O in the biocomposites. In the ^{13}C cross-polarization (CP) MAS NMR spectra (Figure 3c), no distinguishable changes are observed for the aromatic carbon species (C2, C3, C4, and C5) of the TATB ligand before and after enzyme immobilization. ^{13}C NMR signals originating from carbonyl species (C═O) in enzyme molecules can be found at 173 ppm,[71] which overlaps with the C1 ^{13}C CP NMR signal from PCN-333 (Figure 3d). In addition, only tiny ^{13}C resonance peaks originating from the aliphatic carbon of immobilized protein molecules are also detected in Figure 3c ($\delta_{^{13}C}$ = 20−40 ppm) for lipase@PCN-333 and insulin@PCN-333.[71] The coexistence of ^{1}H and ^{13}C signals of the PCN-333 framework and the guest biomolecule in enzyme@PCN-333 samples confirms the successful immobilization of lipase and insulin. This observation is in agreement with the characterization data in Figure 1, Figure S1, and Figure S6. The absence of new carbon species in the ^{13}C CP MAS NMR spectra for PCN-333 biocomposites samples implies that there are no covalent host−guest interactions between the MOF and the enzyme biomolecules. However, after enzyme immobilization, the signal related to the carboxylate carbon (C6) shifts to a higher field ($\delta_{^{13}C}$ = 169 ppm) for both PCN-333 biocomposite samples (see Figure 3d and Table S3 for details). These chemical shifts of the carboxylate C6 species are reported to be an indicative probe for studying the variation in the coordination environment of metal nodes in a metal−organic complex.[72] For example, Ke et al. studied the ssNMR shift of carboxylates carbon of benzoate in $[Cu_2(C_6H_5CO_2)_4]_n$ to determine the nature of the interaction between the Cu-paddle wheel and urea.[73] The authors claimed that upon coordination of urea to the open Cu sites, the chemical signal of the carboxylate carbons in the benzoate ligand shifted to high-fields.[73] In the present study, a high-field shift in ^{13}C signal of carboxylate carbons (C6) is also observed in enzyme@PCN-333 samples (from 171 ppm in PCN-333 to 169 ppm in lipase@PCN-333 and insulin@PCN-333, Figure 3d and Table S3). The high-field shift of C6 is consistent with the literature, indicating a change of the local chemical environment of the Al-oxo clusters in PCN-333 and possible host−guest interaction between the Al-oxo clusters of host PCN-333 and the guest biomolecules. This result is also in good agreement with the information obtained from the ^{27}Al T_1 ssNMR relaxation measurements (Table 1 and Figure S8).

To reveal the existence of interaction between the PCN-333 and the immobilized biomolecules, ^{27}Al MAS NMR technique[74,75] was applied to characterize the local chemical environment of Al nuclei in PCN-333 samples. In the ^{27}Al MAS NMR spectrum, only one broad peak is observed in the region of 8−15 ppm for PCN-333 (Figure 4a and Figure S10). The ^{27}Al peak position indicates the presence of hexa-coordinated Al^{3+} (Al^{VI}) cations[51,76] in PCN-333. After enzyme immobilization, the width of the ^{27}Al peak decreased (Figure S10, as measured by the values of the full width at half-maximum (fwhm), Table S4). This difference in the shape of ^{27}Al spectra further confirms the change in the chemical environment of the Al centers in PCN-333 after enzyme immobilization. These results are consistent with the information obtained via ^{27}Al NMR relaxation spectra (Table 1, Figure S8b). Since ^{27}Al is a quadrupolar nucleus, the strong second-order quadrupolar interaction can lead to broad peaks in the 1D ssNMR spectra and hinder the resolution of subspecies.[77] To obtain detailed information on the Al-oxo cluster, two-dimensional multiple-quantum ^{27}Al MAS NMR spectroscopy (2D ^{27}Al MQ MAS NMR) was applied to resolve the different Al species (Figure S11a−c). For PCN-333, two contour centers for Al^{VI} species with different isotropic chemical shifts are observed (Figure S11a and Table S5), denoted as Al^a ($\delta_{iso^{27}Al}$ = 2.7 ppm) and Al^b ($\delta_{iso^{27}Al}$ = 10.0 ppm). Based on the parameters obtained from 2D ^{27}Al MQ MAS NMR spectra and eqs 1−4 (see Experimental Section for details), the anisotropic 1D ^{27}Al MAS NMR spectra were deconvoluted (Figure 4a). As the peak area of the Al^a is approximately double that of the Al^b species (Al^b/Al^a = 0.48), the Al^a and Al^b species are assigned to Al···OH_2 and AlOH groups, respectively, in the Al-oxo cluster ($Al_3(\mu_3\text{-}O)(OH)(H_2O)_2$). The identification of the two isotropic resonances in the spectra is consistent with the observation reported by Loiseau et al.,[78] who also observed two Al^{VI} species originated from AlOH and Al···OH_2 groups in MIL-110(Al). Importantly, this deconvolution result also matches well with the crystallographic data.[51] After biomolecule loading, no new Al species is observed (Figure S11a−c). Both Al^a and Al^b species remain at

https://doi.org/10.1021/jacsau.1c00226
JACS Au 2021, 1, 2172−2181

similar isotropic chemical shifts with slightly increased quadrupole coupling constant (C_{QCC}) (Table S5). The nonshifted Al^a and Al^b species in peak position confirm the absence of strong coordination interaction at the biointerface. The change in C_{QCC} values of the Al sites points to only a slight distortion in the symmetry of the Al coordination environment (Table S5), which is not strong enough to cause a severe change in the electric field gradients on the Al sites. The small change in quadrupolar coupling constant further confirms the appearance of a new weak interaction between the Al-oxo cluster of the PCN-333 and the biocatalysts. In order to visualize and reveal the nature of the weak interaction between the Al-oxo cluster of the PCN-333 and the biocatalysts in-depth, $^1H/^{27}Al$ transfer of population in double-resonance (TRAPDOR) NMR technique was applied to study the correlation between the Al atoms in PCN-333 and their neighboring protons.[79] Figure 4b shows the amplified $^1H/^{27}Al$ TRAPDOR NMR spectra of PCN-333 samples, in which both Al···OH_2 ($\delta_{^1H}$ = 7−8 ppm) and AlOH ($\delta_{^1H}$ = 2.4 ppm) can be observed. This observation further confirmed the proton assignment in the ^1H spectra (Figure 3b). Interestingly, a strong correlation between the -NH_2 (narrow signal $\delta_{^1H}$ = 5 ppm) and Al nuclei was observed for lipase@PCN-333 and insulin@PCN-33 (Figure 4b). Since the physisorbed water molecule is extremely dynamic compared to other molecules, the majority of the $^1H-^{27}Al$ dipolar couplings between the water molecules and Al-oxo cluster are averaged away. The absence of a sharp peak at $\delta_{^1H}$ = 5 ppm in PCN-333 rules out the possibility that the $^1H-^{27}Al$ correlation observed at 5 ppm for enzyme@PCN-333 samples was derived from the signal between the exchangeable water molecule and Al sites of PCN-333 (Figure 4b and Figure S12). Thus, the identified correlation can be assigned to the $^1H-^{27}Al$ dipolar couplings between the -NH_2 group of the enzymes ($\delta_{^1H}$ = 5 ppm) and Al nuclei of PCN-333. This result clearly indicates the presence of proximity and host−guest interaction between the -NH_2 group of the immobilized biocatalyst and the Al-oxo cluster of the PCN-333. Since no shift of peak position is observed for the -NH_2 group in the $^1H/^{27}Al$ TRAPDOR spectra, there is no strong coordination, hydrogen bonds, or covalent interactions between the Al centers and the -NH_2 functionalities. Thus, with weak van der Waals interaction between the Al sites and -NH_2 sites, the biocatalysts were confined inside the cavities of the PCN-333 and immobilized on the PCN-333 crystal surface in relatively high affinity. In addition, since the signal intensity of the -NH_2 is much stronger than those of the AlOH and Al···OH_2 groups, we conclude that the interaction between the enzyme and PCN-333 is primarily governed by the interactions between the Al-oxo clusters of the host PCN-333 and the -NH_2 moieties of the guest biocatalysts.

All experimental data are consistent with the hypothesis that the confined biocatalysts in PCN-333 are predominantly governed by the interactions between the Al sites of PCN-333 and the -NH_2 functionalities of biocatalysts. The strong $^1H-^{27}Al$ correlation undoubtedly suggests that the host−guest interactions are with -NH_2 functionalities to Al-oxo cluster ($\delta_{^1H}$ = 5.0 ppm in $^1H/^{27}Al$ TRAPDOR spectra). We speculate that surface-exposed lysine or arginine residues of lipase and insulin play a key role in the enzyme−MOF interaction (Figure 4c). Meanwhile, the overall dynamic change (T_1 of ^1H NMR) of enzyme@PCN-333 implies the existence of the confinement effects for immobilized enzymes in MOFs.

CONCLUSION

In conclusion, enzyme biomolecules (lipase and insulin) have been successfully immobilized in PCN-333 MOF and maintained high biocatalytic activity. The change of both the relaxation times and chemical shifts in ssNMR studies indicates that the immobilization of proteins affects both the flexibility and local structure of PCN-333. After enzyme immobilization, the overall framework flexibility was decreased (increase in ^1H T_1 values) due to the confinement effects to enzymes from pores, while the ^{27}Al spin−lattice relaxation time for enzyme@PCN-333 showed a different trend due to the interaction between the Al-oxo cluster in PCN-333 and the biocatalysts. Analysis of the enzyme@PCN-333 revealed that a distinct signal related to the -NH_2 group of the biocatalyst in the ^1H ssNMR spectra is concomitant with a subtle chemical shift of carboxylate ^{13}C spectral feature that is associated with a change of the coordination environment in the Al sites of PCN-333. These data suggest the dominant interactions between the biomolecules and the Al oxo-cluster of PCN-333. Via both $^1H/^{27}Al$ TRAPDOR NMR and multiple quantum ^{27}Al MAS NMR, the immobilization mechanism was further revealed, where the spectroscopic data support the existence of weak interactions between the Al atoms in MOF and the -NH_2 sites on the biocatalysts via van der Waals forces. After combining all the experimental evidence, we, for the first time, have experimentally visualized the immobilization of enzymes in PCN-333 and deduced the possible host−guest interaction mode between the MOF's Al oxo-cluster and the biocatalyst's -NH_2 sites as well as the pore confinement effect. This work shed light on the complex relationship between enzyme and MOF support in the biointerface. In addition, this fundamental knowledge will help to guide the design of other supported enzymatic systems with optimum catalytic activity and stability.

EXPERIMENTAL SECTION

Syntheses

All chemicals and solvents were purchased from commercial sources and used as received without further purification.

Ligand Synthesis. 4,4′,4″-*s*-triazine-2,4,6-triyl-tribenzoate (TATB) was synthesized according to the literature.[51]

PCN-333 Synthesis. PCN-333 was synthesized according to the literature.[51] The as synthesized MOF materials were then washed sequentially with DMF (3 × 2 mL) and ethanol (3 × 2 mL) over 2 days. Thereafter, the PCN-333 was collected by centrifugation and dried in vacuum at room temperature. The dried PCN-333 was stored in a sealed vial at 4 °C before further usage and characterization.

Enzyme@PCN-333 Synthesis. Enzyme@PCN-333 samples were synthesized by mixing lipase (1 mL of 5 mg mL^{-1} lipase aqueous solution) or insulin (1 mL of 5 mg mL^{-1} insulin stock solution) with the as-synthesized PCN-333 (100 mg) at 4 °C for 1 h. The insulin stock solution was prepared by dissolving 5 mg of insulin in 1 mL of diluted HCl solution (pH 3.0, 20 mM). Thereafter, the solid was recovered by centrifugation and washed with H_2O (3 × 1 mL) to remove the excess biomolecule. All supernatants were collected. The concentration of biomolecule in the supernatant was determined by the Bradford assay. The amount of biomolecule immobilized in PCN-333 was calculated by the difference between the concentration used in the synthesis and that in the collected supernatant.

Fluorescein-Tagged Lipase (FITC-Lipase). A solution of fluorescein isothiocyanate (FITC, 0.005 M, 0.0003 mmol) in aqueous carbonate/bicarbonate buffer solution (60 μL, 0.1 M, pH 9.2) was added to a solution of lipase (10 mg, Sigma-Aldrich 62288 lipase from *Pseudomonas cepacia*, 30 units mg^{-1}) in aqueous carbonate/bicarbonate buffer solution (1.94 mL, 0.1 M, pH 9.2) at 0 °C. The solution was covered with aluminum foil and stirred at 0 °C for 4 h.

https://doi.org/10.1021/jacsau.1c00226
JACS Au 2021, 1, 2172−2181

The reaction solution was then filtered through Sephadex G-25M, PD-10 column (GE Healthcare, 17085101), which had been equilibrated with water, eluting with aqueous carbonate/bicarbonate buffer solution (0.1 M, pH 9.2). The fractions containing FITC-lipase were concentrated through a Pall corporation Microsep Advance 10K membrane by centrifugation (4000 rpm; multiple batches were required ∼20 min). The concentrated FITC-lipase was washed twice with deionized water and combined to give a final volume of 2 mL, which was stored at 4 °C, protected from light, until required. The stock solution was assumed to contain 5 mg mL^{-1} of lipase.

FITC-Lipase@PCN-333 Synthesis. A solution of aqueous FITC-lipase (100 μL, 5 mg mL^{-1}) was added to PCN-333 powder (10 mg) at 0 °C. The suspension was stirred at 0 °C for 1 h. The suspension was transferred to an Eppendorf tube, with deionized water and centrifuged (6000 rpm, 2 min). The supernatant was removed, the pellet was resuspended in deionized water and centrifuged as above (×3) to remove the excess FITC-lipase. The pellet was suspended in deionized water (1 mL) to afford a concentration of 0.5 $mg_{FITC\text{-}lipase}$ mL^{-1} with an assumption of 100% FITC-lipase immobilization in PCN-333. The complete immobilization of FITC-lipase was supported by the absence of fluorescence signal (from the FITC tag in the FITC-lipase) in the supernatant from the immobilization mixture. The suspension was stored at 4 °C, protected from light, until required.

Characterization

Gas Sorption. N_2 sorption isotherms were measured on an autosorb iQ (Quantachrome INSTRUMENTS Inc.). Approximately 50 mg of the powdered solid was loaded into a glass analysis tube and outgassed under dynamic vacuum at 60 °C for 12 h. N_2 adsorption and desorption isotherms were measured at 77 K, and data were analyzed using Brunauer−Emmett−Teller (BET) analysis models[80] to determine the surface area. The pore size distribution calculations were carried out using the ASiQwin software DFT package (Quantachrome INSTRUMENTS Inc.).

Powder X-ray Diffraction (PXRD). PXRD measurements were performed on a PANalytical XPert Pro powder diffractometer fitted with a solid-state PIXcel detector (45 kV, 40 mA, 1° divergence and antiscatter slits, and 0.3 mm receiver and detector slits) using Cu Kα (λ = 1.5406 Å) radiation.

Catalytic Assay of FITC-lipase and FITC-lipase@PCN-333. The catalytic activity of the free FITC-lipase or FITC-lipase@PCN-333 was measured according to a modified protocol from Sigma-Aldrich. UV−vis measurements were recorded on a Shimadzu UV-3600i Plus UV−vis−NIR spectrophotometer between the wavelengths of 600 and 300 nm. The enzymatic activity of free FITC-lipase or FITC-lipase@PCN-333 was calculated from the change of absorbance at 400 nm. In a specific experiment with free FITC-lipase, an aqueous solution of FITC-lipase (5 μL, 5 $mg_{FITC\text{-}lipase}$ mL^{-1}) and a solution of 4-nitrophenyl butyrate in acetonitrile (10 μL, 50 mM, 0.5 mmol) were added sequentially into an aqueous Tris-HCl buffer solution (985 μL, 50 mM, pH 7.4) at room temperature. The reaction was left to stand at room temperature for the allocated reaction time before being transferred to a 1 mL cuvette for UV−vis measurement. The absorbance at 400 nm was recorded and used to measure the enzymatic activity of the materials.

For experiments with FITC-lipase@PCN-333, a suspension of FITC-lipase@PCN-333 in deionized water (50 μL, 0.5 $mg_{FITC\text{-}lipase}$ mL^{-1}) was added to a solution of 4-nitrophenyl butyrate in acetonitrile (10 μL, 50 mM, 0.5 mmol) in aqueous Tris-HCl buffer solution (940 μL, 50 mM, pH 7.4) at room temperature. The reaction mixture was left to stand at room temperature before being centrifuged (13 500 RPM, 30 s) before the allocated time. The supernatant was transferred into a 1 mL cuvette, and the absorbance at 400 nm was measured.

Recycling Catalytic Activity of FITC-lipase@PCN-333. Recycling experiments of FITC-lipase@PCN-333 were completed as per the experimental protocol of the catalytic activity of FITC-lipase@PCN-333 mentioned above. Absorbance at 400 nm was collected after a reaction time of 2 min. Between each run, the FITC-lipase@PCN-333 pellet was resuspended in deionized water, centrifuged (13 500 RPM, 30 s) and the supernatant removed (× 2). The next cycle was started upon the addition of a mixture of the 4-nitrophenyl butyrate and Tris-HCl buffer solutions cited above.

Solid-State Magic Angle Spinning NMR Experiments. Prior to the ^1H, ^{13}C, and ^{27}Al MAS NMR experiments, all samples were fully hydrated by exposure to the atmosphere for a week. The single pulse MAS NMR experiments for ^1H, ^{13}C, and ^{27}Al were performed on a Bruker Avance III 500WB spectrometer at a resonance frequency of 400.1 MHz using a 4 mm MAS rotor. For ^1H single-pulse MAS NMR, spinning rate of 12 kHz, 64 scans were recorded for the spectra after single-pulse $\pi/2$ excitation with repetition times of 20 s. ^{13}C and ^{27}Al MAS NMR investigations were conducted at a resonance frequency of 125.7 and 130.3 MHz, respectively. Noteworthy, a spin rate of 10 kHz has been applied for ^{13}C MAS NMR experiments with the purpose of avoiding the overlap of the spinning sidebands from the peaks, while the 12 kHz spinning rate was applied for ^{27}Al MAS NMR measurements. Five thousand scans were recorded to obtain ^{13}C CP MAS NMR spectra with a contact time of 4 ms and a repetition time of 4 s. Single-pulse ^{27}Al MAS NMR spectra were recorded after a single pulse $\pi/6$ excitation with a repetition time of 0.5 s. In order to obtain readable ^{27}Al MAS NMR spectra, 200 scans have been recorded. The two-dimensional (2D) ^{27}Al MQ spectra were acquired using the three-pulse z-filter MQ MAS pulse sequence.[81] The spectra were sheared with TopSpin2.1 xfshear program. The repetition time for the 2D ^{27}Al MQ experiments was 1 s, and 5000 scans were recorded. Parameters of isotropic chemical shift (δ_{iso}), quadrupolar constant (C_{QCC}), and asymmetric parameter (η) have been obtained by applying eqs 1−4 for the 2D MQ MAS spectra[77] with the purpose to obtain information for the decomposition of ^{27}Al MAS NMR spectra:

$$\mathrm{SOQE}^2 = \frac{\delta_{iso} - \delta_{F_2}}{k} \quad (1)$$

$$\delta_{iso} = \frac{17}{27}\delta_{F_1} + \frac{10}{27}\delta_{F_2} \quad (2)$$

$$k = \frac{3}{10}\frac{4I(I+1) - 3}{[4I(2I-1)V_o]^2} \times 10^6 \quad (3)$$

$$\mathrm{SOQE} = C_{QCC}\sqrt{1 + (\eta^2/3)} \quad (4)$$

The values of I (nuclear spin of the quadrupolar nucleus) and V_o (Larmor frequency of the quadrupolar nucleus) were 5/2 and 104.3 MHz, respectively. SOQE represents the second order quadrupolar effect parameter, and δ_{F_1} and δ_{F_2} are the centers of gravity of the MQ MAS signal in the F_1 and F_2 dimension.

Spin−lattice relaxation times (T_1) were determined via ^1H and ^{27}Al detection applying inversion recovery and saturation recovery, with a list of t_1 delay of 10, 5, 4, 3, 2, 1, 0.5, 0.25, 0.1, and 0.01 s for ^1H T_1 value measurements and 120, 100, 80, 40, 20, 10, 5, 2, 1, 0.5, 0.2, 0.1, 0.05, and 0.02 ms for ^{27}Al T_1 value measurements. In the ^1H T_1 experiment, a 180° pulse was applied first to get a fully inverted M_z. A fully recovered equilibrium magnetization (M_z > 99%) can be achieved after a long recycle delay (D_1 = 50 s). Another 90° pulse was then applied to flip the magnetization. For the ^{27}Al T_1 measurement, a 90° pulse was first applied to saturate the system; before the second 90° pulse, a 2 s recycling delay was applied for the magnetization recovery. The corresponding spectra were recorded as a 2D data where the t_1 delay was varied (t_1 delay list). The ^1H T_1 and ^{27}Al T_1 spectral deconvolutions were applied to obtain readable information using the TopSpin and DMFit software.[82] By application of eq 5, the corresponding T_1 values were obtained. In eq 5, M_t represents the original magnetization length, t is the applied t_1 delay, and M represents the magnetization recovery after a specific t_1 delay.[82]

$$M_t = M(1 - e^{-t/T_1}) \quad (5)$$

https://doi.org/10.1021/jacsau.1c00226
JACS Au 2021, 1, 2172−2181

ASSOCIATED CONTENT

Supporting Information

The Supporting Information is available free of charge at https://pubs.acs.org/doi/10.1021/jacsau.1c00226.

Full analytic details, including SEM images, CLSM images, gas sorption isotherms, and ssNMR data (PDF)

AUTHOR INFORMATION

Corresponding Authors

Weibin Liang − *Laboratory for Catalysis Engineering, School of Chemical and Biomolecular Engineering, Sydney Nano Institute, the University of Sydney, Sydney, NSW 2006, Australia;* orcid.org/0000-0002-3032-436X; Email: weibin.liang@sydney.edu.au

Jun Huang − *Laboratory for Catalysis Engineering, School of Chemical and Biomolecular Engineering, Sydney Nano Institute, the University of Sydney, Sydney, NSW 2006, Australia;* orcid.org/0000-0001-8704-605X; Email: jun.huang@sydney.edu.au

Authors

Wenjie Yang − *Laboratory for Catalysis Engineering, School of Chemical and Biomolecular Engineering, Sydney Nano Institute, the University of Sydney, Sydney, NSW 2006, Australia; School of Engineering, Macquarie University, Sydney, NSW 2109, Australia*

Luke A. O'Dell − *Institute for Frontier Materials, Deakin University, Geelong, VIC 3220, Australia;* orcid.org/0000-0002-7760-5417

Hamish D. Toop − *Department of Chemistry and the Centre for Advanced Nanomaterials, The University of Adelaide, Adelaide, South Australia 5005, Australia;* orcid.org/0000-0003-4637-4764

Natasha Maddigan − *Department of Chemistry and the Centre for Advanced Nanomaterials, The University of Adelaide, Adelaide, South Australia 5005, Australia*

Xingmo Zhang − *Laboratory for Catalysis Engineering, School of Chemical and Biomolecular Engineering, Sydney Nano Institute, the University of Sydney, Sydney, NSW 2006, Australia*

Alena Kochubei − *School of Engineering, Macquarie University, Sydney, NSW 2109, Australia*

Christian J. Doonan − *Department of Chemistry and the Centre for Advanced Nanomaterials, The University of Adelaide, Adelaide, South Australia 5005, Australia;* orcid.org/0000-0003-2822-0956

Yijiao Jiang − *School of Engineering, Macquarie University, Sydney, NSW 2109, Australia;* orcid.org/0000-0002-6191-9825

Complete contact information is available at: https://pubs.acs.org/10.1021/jacsau.1c00226

Author Contributions

All authors have given approval to the final version of the manuscript.

Notes

The authors declare no competing financial interest.

ACKNOWLEDGMENTS

This work was supported by the Australian Research Council under the Discovery Projects Schemes (DP180104010, DP170103531, and DP200102411). W.Y. gratefully acknowledges the support of University of Sydney International Scholarship Strategic (USydIS-Strategic). The authors thank Dr. Nicole Cordina for her assistance in the NMR technique support. The authors acknowledge the facilities and the scientific and technical assistance of Sydney Analytical, a core research facility at The University of Sydney. The authors acknowledge the instruments and scientific and technical assistance of Microscopy Australia at Adelaide Microscopy, The University of Adelaide, a facility that is funded by the University and State and Federal Governments.

DEDICATION

Dedicated to Professor Jianzhong Chen on the occasion of his 70th birthday.

REFERENCES

(1) Furukawa, H.; Cordova, K. E.; O'Keeffe, M.; Yaghi, O. M. The chemistry and applications of metal-organic frameworks. *Science* **2013**, *341*, 1230444.

(2) Zhou, H.-C.; Kitagawa, S. Metal-organic frameworks (MOFs). *Chem. Soc. Rev.* **2014**, *43*, 5415.

(3) Maurin, G.; Serre, C.; Cooper, A.; Férey, G. The new age of MOFs and of their porous-related solids. *Chem. Soc. Rev.* **2017**, *46*, 3104−3107.

(4) Kitagawa, S. Porous crystalline materials: closing remarks. *Faraday Discuss.* **2017**, *201*, 395−404.

(5) Rungtaweevoranit, B.; Diercks, C. S.; Kalmutzki, M. J.; Yaghi, O. M. Spiers Memorial Lecture: Progress and prospects of reticular chemistry. *Faraday Discuss.* **2017**, *201*, 9−45.

(6) Dincă, M.; Long, J. R. *Chem. Rev.* **2020**, *120*, 8037−8038.

(7) Doonan, C.; Riccò, R.; Liang, K.; Bradshaw, D.; Falcaro, P. Metal−organic frameworks at the biointerface: synthetic strategies and applications. *Acc. Chem. Res.* **2017**, *50*, 1423−1432.

(8) Riccò, R.; Liang, W.; Li, S.; Gassensmith, J. J.; Caruso, F.; Doonan, C.; Falcaro, P. Metal−organic frameworks for cell and virus biology: a perspective. *ACS Nano* **2018**, *12*, 13−23.

(9) Lian, X.; Fang, Y.; Joseph, E.; Wang, Q.; Li, J.; Banerjee, S.; Lollar, C.; Wang, X.; Zhou, H.-C. Enzyme−MOF (metal−organic framework) composites. *Chem. Soc. Rev.* **2017**, *46*, 3386−3401.

(10) Liang, W.; Wied, P.; Carraro, F.; Sumby, C. J.; Nidetzky, B.; Tsung, C.-K.; Falcaro, P.; Doonan, C. J. Metal−Organic Framework-Based Enzyme Biocomposites. *Chem. Rev.* **2021**, *121*, 1077−1129.

(11) Guillerm, V.; Kim, D.; Eubank, J. F.; Luebke, R.; Liu, X.; Adil, K.; Lah, M. S.; Eddaoudi, M. A supermolecular building approach for the design and construction of metal−organic frameworks. *Chem. Soc. Rev.* **2014**, *43*, 6141−6172.

(12) Jia, F.; Narasimhan, B.; Mallapragada, S. Materials-based strategies for multi-enzyme immobilization and co-localization: a review. *Biotechnol. Bioeng.* **2014**, *111*, 209−222.

(13) Küchler, A.; Yoshimoto, M.; Luginbühl, S.; Mavelli, F.; Walde, P. Enzymatic reactions in confined environments. *Nat. Nanotechnol.* **2016**, *11*, 409.

(14) Herron, N.; Corbin, D. R. *Inclusion Chemistry with Zeolites: Nanoscale Materials by Design*; Springer Science & Business Media: 1995; Vol. *6*.

(15) Bezerra, C. S.; de Farias Lemos, C. M. G.; de Sousa, M.; Gonçalves, L. R. B. Enzyme immobilization onto renewable polymeric matrixes: past, present, and future trends. *J. Appl. Polym. Sci.* **2015**, *132*, 42125.

(16) Kong, G.; Xiong, M.; Liu, L.; Hu, L.; Meng, H.-M.; Ke, G.; Zhang, X.-B.; Tan, W. DNA origami-based protein networks: from

basic construction to emerging applications. *Chem. Soc. Rev.* **2021**, *50*, 1846.
(17) Horcajada, P.; Gref, R.; Baati, T.; Allan, P. K.; Maurin, G.; Couvreur, P.; Ferey, G.; Morris, R. E.; Serre, C. Metal−organic frameworks in biomedicine. *Chem. Rev.* **2012**, *112*, 1232−1268.
(18) Wang, L.; Zheng, M.; Xie, Z. Nanoscale metal−organic frameworks for drug delivery: a conventional platform with new promise. *J. Mater. Chem. B* **2018**, *6*, 707−717.
(19) Sun, H.; Li, Y.; Yu, S.; Liu, J. Metal-organic frameworks (MOFs) for biopreservation: From biomacromolecules, living organisms to biological devices. *Nano Today* **2020**, *35*, 100985.
(20) Liang, W.; Ricco, R.; Maddigan, N. K.; Dickinson, R. P.; Xu, H.; Li, Q.; Sumby, C. J.; Bell, S. G.; Falcaro, P.; Doonan, C. J. Control of structure topology and spatial distribution of biomacromolecules in protein@ ZIF-8 biocomposites. *Chem. Mater.* **2018**, *30*, 1069−1077.
(21) Liang, W.; Xu, H.; Carraro, F.; Maddigan, N. K.; Li, Q.; Bell, S. G.; Huang, D. M.; Tarzia, A.; Solomon, M. B.; Amenitsch, H.; et al. Enhanced activity of enzymes encapsulated in hydrophilic metal−organic frameworks. *J. Am. Chem. Soc.* **2019**, *141*, 2348−2355.
(22) Hanefeld, U.; Gardossi, L.; Magner, E. Understanding enzyme immobilisation. *Chem. Soc. Rev.* **2009**, *38*, 453−468.
(23) Bolivar, J. M.; Eisl, I.; Nidetzky, B. Advanced characterization of immobilized enzymes as heterogeneous biocatalysts. *Catal. Today* **2016**, *259*, 66−80.
(24) Sun, C.; Cheng, Y.; Pan, Y.; Yang, J.; Wang, X.; Xia, F. Efficient polymerase chain reaction assisted by metal−organic frameworks. *Chem. Sci.* **2020**, *11*, 797−802.
(25) Chen, Y.; Jiménez-Ángeles, F.; Qiao, B.; Krzyaniak, M. D.; Sha, F.; Kato, S.; Gong, X.; Buru, C. T.; Chen, Z.; Zhang, X.; et al. Insights into the Enhanced Catalytic Activity of Cytochrome c When Encapsulated in a Metal−Organic Framework. *J. Am. Chem. Soc.* **2020**, *142*, 18576−18582.
(26) Chen, Y.; Jiménez-Ángeles, F.; Qiao, B.; Krzyaniak, M. D.; Sha, F.; Kato, S.; Gong, X.; Buru, C. T.; Chen, Z.; Zhang, X.; Gianneschi, N. C.; Wasielewski, M. R.; Olvera de la Cruz, M.; Farha, O. K. Insights into the Enhanced Catalytic Activity of Cytochrome c When Encapsulated in a Metal−Organic Framework. *J. Am. Chem. Soc.* **2020**, *142*, 18576−18582.
(27) Chen, Y.; Han, S.; Li, X.; Zhang, Z.; Ma, S. Why does enzyme not leach from metal−organic frameworks (MOFs)? Unveiling the interactions between an enzyme molecule and a MOF. *Inorg. Chem.* **2014**, *53*, 10006−10008.
(28) Ashbrook, S. E.; Griffin, J. M.; Johnston, K. E. Recent advances in solid-state nuclear magnetic resonance spectroscopy. *Annu. Rev. Anal. Chem.* **2018**, *11*, 485−508.
(29) Brunner, E.; Lutz, K. Solid-state NMR in biomimetic silica formation and silica biomineralization. *Handbook of biomineralization: biomimetic and bioinspired chemistry* **2007**, *2*, 19−38.
(30) Molugu, T. R.; Lee, S.; Brown, M. F. Concepts and methods of solid-state NMR spectroscopy applied to biomembranes. *Chem. Rev.* **2017**, *117*, 12087−12132.
(31) Ravera, E.; Cerofolini, L.; Martelli, T.; Louka, A.; Fragai, M.; Luchinat, C. 1 H-detected solid-state NMR of proteins entrapped in bioinspired silica: a new tool for biomaterials characterization. *Sci. Rep.* **2016**, *6*, 27851.
(32) Bertmer, M. Solid-state NMR of small molecule adsorption in metal−organic frameworks (MOFs). In *Annual Reports on NMR Spectroscopy*; Atta ur, R., Ed.; Academic Press: 2020; Vol. *101*, Chapter 1, pp 1−64.
(33) Lucier, B. E. G.; Zhang, Y.; Lee, K. J.; Lu, Y.; Huang, Y. Grasping hydrogen adsorption and dynamics in metal−organic frameworks using 2H solid-state NMR. *Chem. Commun.* **2016**, *52*, 7541−7544.
(34) Ueda, T.; Kurokawa, K.; Eguchi, T.; Kachi-Terajima, C.; Takamizawa, S. Local Structure and Xenon Adsorption Behavior of Metal−Organic Framework System [M2(O2CPh)4(pyz)]n (M = Rh and Cu) As Studied with Use of Single-Crystal X-ray Diffraction, Adsorption Isotherm, and Xenon-129 NMR. *J. Phys. Chem. C* **2007**, *111*, 1524−1534.
(35) Wong, Y. T. A.; Babcock, T. K.; Chen, S.; Lucier, B. E. G.; Huang, Y. CO Guest Interactions in SDB-Based Metal−Organic Frameworks: A Solid-State Nuclear Magnetic Resonance Investigation. *Langmuir* **2018**, *34*, 15640−15649.
(36) Kong, X.; Scott, E.; Ding, W.; Mason, J. A.; Long, J. R.; Reimer, J. A. CO2 Dynamics in a Metal−Organic Framework with Open Metal Sites. *J. Am. Chem. Soc.* **2012**, *134*, 14341−14344.
(37) Forse, A. C.; Milner, P. J.; Lee, J.-H.; Redfearn, H. N.; Oktawiec, J.; Siegelman, R. L.; Martell, J. D.; Dinakar, B.; Porter-Zasada, L. B.; Gonzalez, M. I.; Neaton, J. B.; Long, J. R.; Reimer, J. A. Elucidating CO2 Chemisorption in Diamine-Appended Metal−Organic Frameworks. *J. Am. Chem. Soc.* **2018**, *140*, 18016−18031.
(38) Khan, A. H.; Barth, B.; Hartmann, M.; Haase, J. r.; Bertmer, M. Nitric oxide adsorption in MIL-100 (Al) MOF studied by solid-state NMR. *J. Phys. Chem. C* **2018**, *122*, 12723−12730.
(39) Gul-E-Noor, F.; Jee, B.; Pöppl, A.; Hartmann, M.; Himsl, D.; Bertmer, M. Effects of varying water adsorption on a Cu 3 (BTC) 2 metal−organic framework (MOF) as studied by 1 H and 13C solid-state NMR spectroscopy. *Phys. Chem. Chem. Phys.* **2011**, *13*, 7783−7788.
(40) Li, J.; Li, S.; Zheng, A.; Liu, X.; Yu, N.; Deng, F. Solid-state NMR Studies of Host−Guest Interaction between UiO-67 and Light Alkane at Room Temperature. *J. Phys. Chem. C* **2017**, *121*, 14261−14268.
(41) Khudozhitkov, A. E.; Jobic, H.; Kolokolov, D. I.; Freude, D.; Haase, J. r.; Stepanov, A. G. Probing the guest-mediated structural mobility in the UiO-66 (Zr) framework by 2H NMR spectroscopy. *J. Phys. Chem. C* **2017**, *121*, 11593−11600.
(42) Khudozhitkov, A. E.; Arzumanov, S. S.; Kolokolov, D. I.; Stepanov, A. G. Mobility of Aromatic Guests and Isobutane in ZIF-8 Metal−Organic Framework Studied by 2H Solid State NMR Spectroscopy. *J. Phys. Chem. C* **2019**, *123*, 13765−13774.
(43) Torres-Huerta, A.; Galicia-Badillo, D.; Aguilar-Granda, A.; Bryant, J. T.; Uribe-Romo, F. J.; Rodríguez-Molina, B. Multiple rotational rates in a guest-loaded, amphidynamic zirconia metal−organic framework. *Chem. Sci.* **2020**, *11*, 11579−11583.
(44) Tang, J.; Li, S.; Chu, Y.; Xiao, Y.; Xu, J.; Deng, F. Host−Guest Interaction between Methanol and Metal−Organic Framework Cu3−xZnx(btc)2 as Revealed by Solid-State NMR. *J. Phys. Chem. C* **2019**, *123*, 24062−24070.
(45) Wittmann, T.; Mondal, A.; Tschense, C. B. L.; Wittmann, J. J.; Klimm, O.; Siegel, R.; Corzilius, B.; Weber, B.; Kaupp, M.; Senker, J. Probing Interactions of N-Donor Molecules with Open Metal Sites within Paramagnetic Cr-MIL-101: A Solid-State NMR Spectroscopic and Density Functional Theory Study. *J. Am. Chem. Soc.* **2018**, *140*, 2135−2144.
(46) Xiao, D.; Xu, S.; Brownbill, N. J.; Paul, S.; Chen, L.-H.; Pawsey, S.; Aussenac, F.; Su, B.-L.; Han, X.; Bao, X.; Liu, Z.; Blanc, F. Fast detection and structural identification of carbocations on zeolites by dynamic nuclear polarization enhanced solid-state NMR. *Chem. Sci.* **2018**, *9*, 8184−8193.
(47) Wang, C.; Chu, Y.; Xu, J.; Wang, Q.; Qi, G.; Gao, P.; Zhou, X.; Deng, F. Extra-Framework Aluminum-Assisted Initial C−C Bond Formation in Methanol-to-Olefins Conversion on Zeolite H-ZSM-5. *Angew. Chem., Int. Ed.* **2018**, *57*, 10197−10201.
(48) Omegna, A.; van Bokhoven, J. A.; Prins, R. Flexible Aluminum Coordination in Alumino−Silicates. Structure of Zeolite H−USY and Amorphous Silica−Alumina. *J. Phys. Chem. B* **2003**, *107*, 8854−8860.
(49) Liu, N.; Higashi, K.; Kikuchi, J.; Ando, S.; Kameta, N.; Ding, W.; Masuda, M.; Shimizu, T.; Ueda, K.; Yamamoto, K.; Moribe, K. Molecular-Level Understanding of the Encapsulation and Dissolution of Poorly Water-Soluble Ibuprofen by Functionalized Organic Nanotubes Using Solid-State NMR Spectroscopy. *J. Phys. Chem. B* **2016**, *120*, 4496−4507.
(50) Alonso, B.; Marichal, C. Solid-state NMR studies of micelle-templated mesoporous solids. *Chem. Soc. Rev.* **2013**, *42*, 3808−3820.
(51) Feng, D.; Liu, T.-F.; Su, J.; Bosch, M.; Wei, Z.; Wan, W.; Yuan, D.; Chen, Y.-P.; Wang, X.; Wang, K.; et al. Stable metal-organic

https://doi.org/10.1021/jacsau.1c00226
JACS Au 2021, 1, 2172−2181

frameworks containing single-molecule traps for enzyme encapsulation. *Nat. Commun.* **2015**, *6*, 5979.
(52) Lian, X.; Erazo-Oliveras, A.; Pellois, J.-P.; Zhou, H.-C. High efficiency and long-term intracellular activity of an enzymatic nanofactory based on metal-organic frameworks. *Nat. Commun.* **2017**, *8*, 2075.
(53) Phipps, J.; Chen, H.; Donovan, C.; Dominguez, D.; Morgan, S.; Weidman, B.; Fan, C.; Beyzavi, M. H. Catalytic Activity, Stability, and Loading Trends of Alcohol Dehydrogenase Enzyme Encapsulated in a Metal−Organic Framework. *ACS Appl. Mater. Interfaces* **2020**, *12*, 26084.
(54) Kim, K. K.; Song, H. K.; Shin, D. H.; Hwang, K. Y.; Suh, S. W. The crystal structure of a triacylglycerol lipase from Pseudomonas cepacia reveals a highly open conformation in the absence of a bound inhibitor. *Structure* **1997**, *5*, 173−185.
(55) Chen, Y.; Li, P.; Modica, J. A.; Drout, R. J.; Farha, O. K. Acid-resistant mesoporous metal−organic framework toward oral insulin delivery: Protein encapsulation, protection, and release. *J. Am. Chem. Soc.* **2018**, *140*, 5678−5681.
(56) Domínguez de Maria, P.; Sánchez-Montero, J. M.; Sinisterra, J. V.; Alcántara, A. R. Understanding Candida rugosa lipases: an overview. *Biotechnol. Adv.* **2006**, *24*, 180−196.
(57) Alberti, K. G. M. M.; Zimmet, P. Z. Definition, diagnosis and classification of diabetes mellitus and its complications. Part 1: diagnosis and classification of diabetes mellitus. Provisional report of a WHO Consultation. *Diabet. Med.* **1998**, *15*, 539−553.
(58) Bradford, N. A rapid and sensitive method for the quantitation microgram quantities of a protein isolated from red cell membranes. *Anal. Biochem.* **1976**, *72*, 248−254.
(59) Zhao, X.; Xiao, B.; Fletcher, A. J.; Thomas, K. M.; Bradshaw, D.; Rosseinsky, M. J. Hysteretic adsorption and desorption of hydrogen by nanoporous metal-organic frameworks. *Science* **2004**, *306*, 1012−1015.
(60) Martinez-Bulit, P.; Stirk, A. J.; Loeb, S. J. Rotors, motors, and machines inside metal−organic frameworks. *Trends Chem.* **2019**, *1*, 588−600.
(61) Marangoni, A.; Al-Abdul-Wahid, M.; Nicholson, R.; Roma, A.; Gravelle, A.; De Souza, J.; Barbut, S.; Spagnuolo, P. Water immobilization by glass microspheres affects biological activity. *Sci. Rep.* **2018**, *8*, 9744.
(62) Hohwy, M.; Jaroniec, C.; Reif, B.; Rienstra, C.; Griffin, R. Local structure and relaxation in solid-state NMR: accurate measurement of amide N− H bond lengths and H− N− H bond angles. *J. Am. Chem. Soc.* **2000**, *122*, 3218−3219.
(63) Lewandowski, J. R. Advances in solid-state relaxation methodology for probing site-specific protein dynamics. *Acc. Chem. Res.* **2013**, *46*, 2018−2027.
(64) Bloembergen, N.; Purcell, E. M.; Pound, R. V. Relaxation effects in nuclear magnetic resonance absorption. *Phys. Rev.* **1948**, *73*, 679.
(65) Okada, K.; Hirai, D.; Kumada, S.; Kosugi, A.; Hayashi, Y.; Onuki, Y. 1H NMR relaxation study to evaluate the crystalline state of active pharmaceutical ingredients containing solid dosage forms using time domain NMR. *J. Pharm. Sci.* **2019**, *108*, 451−456.
(66) Haouas, M.; Volkringer, C.; Loiseau, T.; Férey, G.; Taulelle, F. The Extra-Framework Sub-Lattice of the Metal−Organic Framework MIL-110: A Solid-State NMR Investigation. *Chem. - Eur. J.* **2009**, *15*, 3139−3146.
(67) Grube, E.; Nielsen, U. G. The stoichiometry of synthetic alunite as a function of hydrothermal aging investigated by solid-state NMR spectroscopy, powder X-ray diffraction and infrared spectroscopy. *Phys. Chem. Miner.* **2015**, *42*, 337−345.
(68) Tang, Y.; Huang, H.; Li, J.; Xue, W.; Zhong, C. IL-induced formation of dynamic complex iodide anions in IL@ MOF composites for efficient iodine capture. *J. Mater. Chem. A* **2019**, *7*, 18324−18329.
(69) Jiang, Y.; Huang, J.; Marx, S.; Kleist, W.; Hunger, M.; Baiker, A. Effect of dehydration on the local structure of framework aluminum atoms in mixed linker MIL-53 (Al) materials studied by solid-state NMR spectroscopy. *J. Phys. Chem. Lett.* **2010**, *1*, 2886−2890.
(70) Tay, H. M.; Rawal, A.; Hua, C. S-Mg 2 (dobpdc): a metal−organic framework for determining chirality in amino acids. *Chem. Commun.* **2020**, *56*, 14829−14832.
(71) Varghese, S.; Halling, P. J.; Häussinger, D.; Wimperis, S. High-Resolution Structural Characterization of a Heterogeneous Biocatalyst Using Solid-State NMR. *J. Phys. Chem. C* **2016**, *120*, 28717−28726.
(72) Brunner, E.; Rauche, M. Solid-state NMR spectroscopy: an advancing tool to analyse the structure and properties of metal−organic frameworks. *Chem. Sci.* **2020**, *11*, 4297−4304.
(73) Ke, Z.; Jamieson, L. E.; Dawson, D. M.; Ashbrook, S. E.; Bühl, M. NMR chemical shifts of urea loaded copper benzoate. A joint solid-state NMR and DFT study. *Solid State Nucl. Magn. Reson.* **2019**, *101*, 31−37.
(74) Ehresmann, J. O.; Wang, W.; Herreros, B.; Luigi, D.-P.; Venkatraman, T.; Song, W.; Nicholas, J. B.; Haw, J. F. Theoretical and experimental investigation of the effect of proton transfer on the 27Al MAS NMR line shapes of zeolite− adsorbate complexes: an independent measure of solid acid strength. *J. Am. Chem. Soc.* **2002**, *124*, 10868−10874.
(75) Ganapathy, S.; Gore, K.; Kumar, R.; Amoureux, J.-P. Multinuclear (27Al, 29Si, 47, 49Ti) solid-state NMR of titanium substituted zeolite USY. *Solid State Nucl. Magn. Reson.* **2003**, *24*, 184−195.
(76) Xu, M.; Shen, Y.; Wang, L.; Gong, C.; Chen, S. A Novel H2O2 Biosensor Based On the composite of MP-11 encapasulated in PCN-333 (Al)-Graphene Oxide. *Int. J. Electrochem. Sci.* **2017**, *12*, 10390−10401.
(77) Wang, Z.; Jiang, Y.; Yi, X.; Zhou, C.; Rawal, A.; Hook, J.; Liu, Z.; Deng, F.; Zheng, A.; Hunger, M.; et al. High population and dispersion of pentacoordinated AlV species on the surface of flame-made amorphous silica-alumina. *Sci. Bull.* **2019**, *64*, 516−523.
(78) Volkringer, C.; Popov, D.; Loiseau, T.; Guillou, N.; Ferey, G.; Haouas, M.; Taulelle, F.; Mellot-Draznieks, C.; Burghammer, M.; Riekel, C. A microdiffraction set-up for nanoporous metal−organic-framework-type solids. *Nat. Mater.* **2007**, *6*, 760−764.
(79) Wilke, C.; Chang, P. Correlation of diffusion coefficients in dilute solutions. *AIChE J.* **1955**, *1*, 264−270.
(80) Brunauer, S.; Emmett, P. H.; Teller, E. Adsorption of gases in multimolecular layers. *J. Am. Chem. Soc.* **1938**, *60*, 309−319.
(81) Amoureux, J.-P.; Fernandez, C.; Steuernagel, S. ZFiltering in MQMAS NMR. *J. Magn. Reson., Ser. A* **1996**, *123*, 116.
(82) Massiot, D.; Fayon, F.; Capron, M.; King, I.; Le Calvé, S.; Alonso, B.; Durand, J. O.; Bujoli, B.; Gan, Z.; Hoatson, G. Modelling one-and two-dimensional solid-state NMR spectra. *Magn. Reson. Chem.* **2002**, *40*, 70−76.

https://doi.org/10.1021/jacsau.1c00226
JACS Au 2021, 1, 2172−2181